Well-formed, size-controlled ruthenium nanoparticles active and stable for acetic acid steam reforming

Filippo Bossola [a,b], Claudio Evangelisti [b], Mattia Allieta [c], Rinaldo Psaro [b], Sandro Recchia [a], Vladimiro Dal Santo [b,*]

[a] Dipartimento di Scienza e Alta Tecnologia, Università dell'Insubria, Como 20133, Italy
[b] CNR- Istituto di Scienze e Tecnologie Molecolari, Via Golgi 19, Milano 20133, Italy
[c] Università degli studi di Milano, Dipartimento di Chimica, Via C. Golgi 19, Milano I-20133, Italy

ARTICLE INFO

ABSTRACT

Mg(Al)O supported Ru and Rh catalysts with low loading of active metal (0.5 wt.%) were tested in the steam reforming (SR) of acetic acid (AA) to hydrogen rich mixtures. Two synthetic procedures were adopted to deposit metal nanoparticles on support material: conventional impregnation from metal chlorides aqueous solutions and size-controlled metal nanoparticles (SCMNPs) deposition method. SCMNP derived Ru catalysts showed good performances fully comparable to standard Rh based systems. After 20 h t.o.s. at reaction temperature of 700 °C, steam-to-carbon ratio of 3 and weight hourly space velocity of 6 h^{-1}, Ru catalysts showed 100% conversion and hydrogen yield higher than 70%. The presence of well formed metal nanoparticles and the residual hydrotalcite present in the support play a determinant role in limiting the deactivation by coke deposition and by nanoparticles sintering.

© 2015 Elsevier B.V. All rights reserved.

1. Introduction

Hydrogen is often indicated as one of the possible future energy vectors with low emissions and high efficiency. Nowadays H_2 is mainly produced by steam reforming of fossil fuels. However, hydrogen production processes sustainable from both economic and environmental points of view are a prerequisite for the widespread diffusion of H_2-based technologies. On the other hand, several processes based on renewable energy sources and on renewable/waste raw materials, such as water electrolysis (using electricity obtained from renewable sources) [1,2], and water photo-splitting [3,4] have been proposed. In spite of the fully sustainability of these technologies, several issues, related to scaling up and maximum hydrogen amount that can be produced, make them far from practical application in a short medium timescale. Conversely, reforming processes based on renewable raw materials have high potential because they are based on a well known technology, they are easy to be scaled up, and they are able to provide high productivities. Examples of real applications, at least at pilot plant scale, are already known, such as Linde plant for glyc-erol pyro-steam reforming in Leunde able to produce $50\,m^3\,h^{-1}$ of hydrogen [5], or BTG Biomass Technology Group BV pilot plant for the conversion of wet biomass and residues in supercritical water to produce substitute natural gas (SNG) or hydrogen (able to process $5\text{–}30\,L\,h^{-1}$ of liquids) [6].

Among renewable or waste raw materials pyrolysis oils can play an important role since they can be obtained from a large variety of sources and they are a way to compact biomass therefore improving energy density, lowering water content and making transport, storage and delivery easier. Moreover, pyrolysis oils are complex mixtures of different compounds such as acids, alcohols, ketones, aldehydes, esters, sugars, phenols, and others, thus representing a convenient secondary raw material for the production of several biomaterials, chemicals, biofuels, and energy too.

Hydrogen and syngas are typical products that can be gained from steam reforming of whole bio-oils, or mostly of their hydro-soluble light fraction. The former can be used as energy vector or for up-grading the heavier compounds of non-water soluble fraction of bio-oil, whereas syngas is a key intermediate for the production of biofuels and other chemicals.

Carboxylic acids represent around 4–15% of whole bio-oils [7], acetic acid being one of the main components. It represents around 6–10% of whole bio-oils [8], and reaches up to 12% of water soluble fraction. It is widely used as model compound in the most part of studies devoted to catalyst development.

* Corresponding author. Fax: +39 02 50314405.
E-mail addresses: filippo.bossola@uninsubria.it (F. Bossola),
c.evangelisti@istm.cnr.it (C. Evangelisti), mattia.allieta@gmail.com (M. Allieta),
r.psaro@istm.cnr.it (R. Psaro), v.dalsanto@istm.cnr.it (V. Dal Santo).

Several catalysts based on noble, non-noble metals and also mixtures of them have been reported so far in the literature.

Among noble metals, Rh is known to be one of the most active one [9,10] and ceria–zirconia are globally reported as the most efficient supports due to higher oxygen mobility. Lemonidou and co-workers reported on the optimized performances of a low loaded Rh catalyst supported on (La-doped) CeO_2–ZrO_2 [11,12].

Ru based catalysts are reported to be very active, [13–16] due to their ability in promoting steam-reforming and limiting coke deposition. Conversely, Pt based systems are reported to be less active than Ru, Pd and Rh [17].

On the other hand, among non-noble metals, Ni is the most widely employed, alone [18,19], or in bimetallic systems [20–24].

Conversely to noble metals based catalysts, non-noble systems, mainly Ni and Co ones, cause concerns related to coke deposition. That is one of the main issue for all reforming catalysts [25–28], in particular Hu et al. [29] reported a coke deposition rate of 12.5 mg_{coke} g_{cat}^{-1} h^{-1} for a Ni/Al_2O_3 catalyst after 20 h of steam reforming reaction performed at stoichiometric S/C ratio and T_{REACT} = 600 °C. This negative behavior can be limited by some strategies, such as addition of other metals with a lower carbon–metal bonding energy, like Cu [30] and/or by a proper choice of the support material able to stabilize metal particles, to have high oxygen mobility, and to show a good balance of acidic and basic surface properties.

In this scenario Mg(Al)O mixed oxides are well established support materials in SR reactions of CH_4, ethanol, glycerol, acetic acid, due to their ability in stabilizing supported metal NPs, and limiting coke formation [14,31–39].

Thus, the development of catalysts with high stability and resistance to coke deposition, is a task worth to be pursued. Moreover, to avoid, or limit the amount of noble metal(s) present is another relevant issue.

The development of new preparation approaches based on the synthesis of stabilized metal particles in solution as precursors of heterogeneous catalysts offers the advantage to strictly control the size and the shape of the supported metal nanoparticles [40].

Here we report, for the first time, the application of size-controlled metal nanoparticles (SCMNPs) deposition method [41–45] for the preparation of low loaded Mg(Al)O mixed oxide supported Rh and Ru catalysts and their application in acetic acid steam reforming.

Ruthenium was chosen as active metal due to its good activity in steam reforming, low coke deposition and, if compared, to other noble metals for its lower cost. On the other hand, Mg(Al)O mixed oxides are widely used as support materials in steam reforming, and in particular also with Ru [37,46–48]. Conversely, Rh-based catalysts were taken as reference ones due to their high activity. Rh and Ru nanoparticles were obtained by reduction of the corresponding metal salts with molecular hydrogen in organic phase in the presence of long chain aliphatic amines (e.g., trioctylamine). The prepared colloids were further easily deposited on the support leading to size-controlled supported Rh and Ru nanoparticles, respectively. The advantages of this preparation method, if compared with traditional impregnation, will be demonstrated as activity, stability and coke resistance are taken into account. Moreover, the SCMNPs deposition method here reported can be easily scaled up improving its applicability to potentially real catalysts.

2. Materials and methods

2.1. Catalysts preparation

Mg(Al)O mixed oxide (hereinafter indicated as MG70) support was obtained by calcination in air at 900 °C overnight of the commercial Pural MG70 hydrotalcite (Sasol, Germany).

A first set of catalysts, hereinafter referred to as M/MG70 (M = Rh and Ru), was prepared by wet impregnation method [37], starting from MCl_3 (Sigma–Aldrich) aqueous solutions, followed by calcination in air at 500 °C for 1 h. Another set of catalysts, hereinafter called M(TOA)/MG70, was synthesized by the size-controlled metal nanoparticles (SCMNPs) deposition method [41,42,44]. The SCM-NPs THF solutions (1.7×10^{-3} M) were obtained by reduction of the metal chloride with trioctylamine (TOA) in a slight molar excess (3:1 TOA:M molar ratio) under static hydrogen atmosphere (1.0 bar, T = 25 °C) for 24 h. The SCMNPs were deposited on MG70 by contacting the solutions with the support under inert atmosphere for 1 h, the catalysts were then filtered, washed with THF (3 times, 20 mL) and finally dried in vacuo overnight.

The catalysts were pelletized, crushed and sieved collecting the fraction of 45–35 mesh. Finally, before performing catalytic tests, all catalysts were reduced in situ at 700 °C under H_2 flow (30 mL min^{-1}) for 1 h.

2.2. Materials characterization

Ru loadings were determined by inductively coupled plasma–optical emission spectrometry (ICP–OES) (ICAP 6300 Duo, Thermo Fisher Scientific), after digestion of the catalysts. The reduced Ru catalysts (approximately 15 mg) were digested in 5 mL of NaOCl 13%, and then acidified with 5 mL of HCl 37%. Rh catalysts (approximately 15 mg) were microwave digested in aqua regia. After digestion all solutions were diluted with high purity deionized (18 MΩ cm) water (MilliQ Academic, Millipore) until they reached 20 g. Finally, support residues, eventually present, were eliminated by filtration with a PTFE syringe filter (0.20 μm).

Specific surface areas of supports and catalysts were measured with the BET technique by using a ASAP-2020 apparatus (Micromeritics), employing nitrogen as the adsorbent at −196 °C (77 K). Prior to each measurement, the samples were outgassed at 200 °C for 2 h.

The acid properties of the Ru catalysts were studied by fast Fourier infrared spectroscopy (FT-IR) (Biorad FTS-60A) using pyridine as probe molecule. The reduced samples (700 °C, 1 h in H_2 flow 30 mL min^{-1}) were pressed in a 13 mm diameter pellets, transferred to the IR-cell, which was then sealed, and in situ reduced in static hydrogen atmosphere for 30 min at 500 °C. The samples were then contacted with pyridine vapors at room temperature, followed by 30 min in high vacuum to eliminate the excess of pyridine. The pyridine desorption was carried out stepwise in high vacuum from 50 °C to 250 °C, recording a spectrum, at RT, every 50 °C. Acidic surface sites were determined integrating the peak at 1448 cm^{-1}, corresponding to Lewis acidity (Brønsted acid sites were not detected), according to Emeis [49]. The values are expressed as micromoles of adsorbed pyridine per gram of catalyst (μmol g_{cat}^{-1}).

2.2.1. XRPD

X-ray powder diffraction (XRPD) patterns were recorded in the $5° \leq 2\theta \leq 70°$ range employing the Cu-Kα radiation at room temperature. Rietveld analysis was performed using the GSAS software suite of programs [50]. Structural models were taken from [51] for cubic $MgAl_2O_4$ (space group Fd-3m), from [52] for cubic MgO (Fm-3m) and from [53] for rhombohedral $Mg_6Al_2CO_3(OH)_{16}\cdot4H_2O$ (hereafter HT) (space group R-3m). The background was subtracted using the shifted Chebyshev polynomials and the diffraction peak profiles were fitted with a modified pseudo-Voigt function. In the last refinement cycles, scale phase factors, cell parameters and isotropic thermal parameters were allowed to vary as well as background, zero diffractometer position and line profile parameters.

2.2.2. H₂ TPR

The temperature programmed reduction (TPR) experiments were carried out in a PulseChemisorb 2700 (Micromeritics) device by heating the sample until 750 °C at 8 °C min⁻¹ in 8 vol.% H_2/Ar mixture flow (20 mL min⁻¹). The amount of H_2 consumed was measured by a TCD.

Before analysis, the M/MG70 samples were treated at 130 °C for 1 h under Ar flow (20 mL min⁻¹), while M(TOA)/MG70 samples were calcined at 500 °C for 2 h in O_2 (40 mL min⁻¹).

2.2.3. HRTEM

Electron micrographs were carried out with a Zeiss LIBRA 200FE, equipped with: 200 kV FEG, in column second-generation omega filter for energy selective spectroscopy (EELS) and imaging (ESI), HAADF STEM facility, EDS probe for chemical analysis. Before introduction in the instrument, the samples were ultrasonically dispersed in isopropyl alcohol and a drop of the suspension was deposited on a holey carbon gold grid (300 mesh). The histograms of the metal particle size distribution for the samples were obtained by counting at least 500 particles onto the micrographs. The mean particle diameter (d_m) was calculated by using the formula $d_m = \sum d_i n_i / \sum n_i$, where n_i is the number of particles with diameter d_i. Metal dispersion was evaluated from mean particle diameter according to the procedure reported by Borodziński and Bonarowska [54].

2.2.4. TG analysis

The coke deposited on the catalysts was estimated by thermal gravimetric analysis (TGA) (NETZSCH STA 409 PC/PG). About 40 mg of sample were loaded in a platinum crucible and heated in a 40 mL min⁻¹ air flow up to 900 °C at a constant rate of 5 °C min⁻¹.

2.2.5. CO-DRIFTS

Probe molecule CO adsorption diffuse reflectance infrared Fourier transformed spectroscopy (CO-DRIFTS) experiments were performed using a home-made DRIFTS cell inserted in a Biorad FTS-60A spectrometer and connected upstream to a gas feeding apparatus and downstream to a QMS (Hiden, HPR). The whole apparatus was already described elsewhere [55,56]. Before CO adsorption the samples were reduced in situ in H_2 flow (20 mL min⁻¹) at 500 °C for 1 h, then cooled down to RT in He flow (20 mL min⁻¹). Pure CO flow (20 mL min⁻¹) was then admitted to the DRIFTS reaction chamber and after 30 min the cell was purged with He until CO adsorption bands stability.

2.3. Catalytic tests

Acetic acid SR experiments were carried out in a home-made lab scale testing rig, described elsewhere [37], operating with a fixed bed atmospheric pressure quartz reactor fed with a water/acetic acid solution by means of a dosing pump (KNF LAB SIMDOS 02), He was used as carrier gas (30 mL min⁻¹). Before each test, catalysts (pellets, 45–35 mesh) were reduced at 700 °C for 1 h in H_2 flow (30 mL min⁻¹). Feeding mixture was vaporized on a quartz chunks bed placed before the catalytic bed and heated by a dedicated furnace at 250 °C. Gaseous products (H_2, CO_2, CO and CH_4) were analyzed by an online double column GC-TCD (Agilent 6890N), one analysis per hour (20 analysis per run ca.). The overall reaction and the equations used for the calculation of the H_2 yield, carbon conversion and product selectivities are as follows:

$$CH_3COOH + 2H_2O \rightarrow 2CO_2 + 4H_2$$
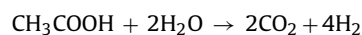
$$H_2\,Yield\ (\%) = \frac{H_2\ mol\ produced}{(mol\ AA\ in\ the\ feed) \times 4} \times 100$$

$$Carbon\ Conversion\ (\%) = \frac{(CO_2 + CO + CH_4)mol\ produced}{(mol\ AA\ in\ the\ feed) \times 2} \times 100$$

$$Selectivity\ of\ i\ (\%) = \frac{i\ mol\ produced}{(\Sigma\ i\ species)\ mol\ produced} \times 100$$

i species = CO_2, CO, CH_4

The catalytic tests were conducted for 20 h of t.o.s. at a reforming temperature (T_R) of 700 °C using a H_2O/AA solution at a steam-to-carbon (S/C) ratio of 3 (mol/mol), fed at 60 μL min⁻¹. The weight hourly space velocity (WHSV) was 6 h⁻¹ (mass of acetic acid in the feed solution per mass of catalyst per hour), but stress tests were conducted at WHSV of 12 h⁻¹ and/or at T_R of 600 °C.

TOF values were calculated as the ratio:

$$TOF\ (h^{-1}) = \frac{mol_{AA}converted\ to\ CO_2, CO, CH_4}{mol_{metal} \times dispersion \times h}$$

metal = Rh, Ru

3. Results

3.1. Catalysts characterization

3.2. General features

Experimental metals loadings, determined by mineralization and ICP-OES analysis, are close to theoretical ones (0.5 wt.%) and ranges from 0.4 to 0.6 wt.% for SCMNPs derived and impregnated catalysts, respectively. Specific surface area of catalysts shows a small decrease with respect to parent bare support, and data suggest dependence on metal content and on calcination times (24 h for MG70 and 48 h for MG70-48, respectively) (see Table 1).

The presence of nitrogen, deriving from decomposition of TOA ligand eventually present in Ru(TOA) and Rh(TOA)/MG70 catalyst was checked by elemental analysis (Table 1). Only Ru(TOA)/MG70 and Ru(TOA)/MG70-48 fresh (i.e., as synthesized) catalysts show a N content of 1.64 and 1.89 wt.%, respectively. However, the reduction treatment completely eliminates the TOA, and the N content in reduced catalysts is close to zero.

The presence of surface acid properties was investigated by pyridine FT-IR. Upon pyridine adsorption bands located around 1600–1613 cm⁻¹ and 1440–1449 cm⁻¹ appear in FTIR spectra (not shown) due to pyridine adsorbed on Mg^{2+} and Al^{3+} sites. More in detail band at 1600–1613 cm⁻¹ originates from Mg^{2+} c.u.s. sites, while that at 1440–1449 cm⁻¹ derives from octahedral and tetrahedral Al^{3+} sites [57]. Only Lewis acidic sites (LAS) were detected in FTIR spectra of adsorbed pyridine, present in comparable amounts (see Table 1) on bare support and on all the reduced Rh and Ru catalysts, regardless the metal and/or preparation method.
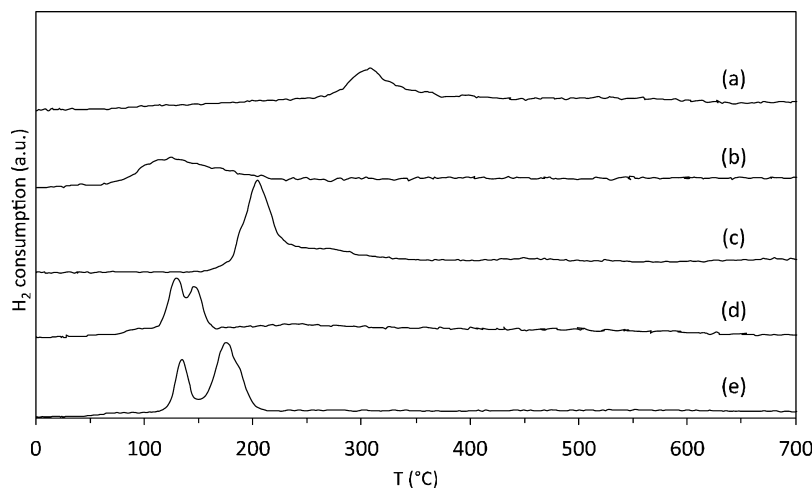
3.3. Temperature programmed reduction (TPR)

TPR profiles of Ru, Rh catalysts are shown in Fig. 1. SCMNPs (M = Ru and Rh) deposited samples show lower reduction temperatures if compared with traditional wet impregnated ones: 304 °C and 122 °C for Rh/MG70 (trace a) and Rh(TOA)/MG70 (trace b), respectively. Ru-based catalysts show a similar behavior, but with a little more complex reduction patterns. Ru/MG70 sample (trace c) has a main peak centered around 204 °C and a small, broad shoulder at 267 °C; Ru(TOA)/MG70 catalyst (trace d) displays two sharp peaks at 128 °C and 145 °C (with also two minor peaks at 90 °C and 233 °C).

Reduction peaks location of MG70 supported SCMNPs closely resembles the peaks found for unsupported NPs (traces b, d and e in Fig. 1), suggesting a lower degree of Ru and Rh cations dissolution in Mg Al spinel lattice or, in other words, a lower interaction of oxide species with support, in oxidized catalysts [37,58].

Table 1
Metal loadings, specific surface area (SSA), N content and Lewis acid sites (LAS) of bare MG70 support and of Rh and Ru catalysts.

Sample	M (Rh, Ru) loadings (wt.%)	SSA_{BET} (m^2 g^{-1})	N content fresh/reduced (wt.%)	LAS (μmol g_{cat}^{-1})
MG70	–	87	0/0	16
Rh/MG70	0.51	75	0/0	19
Rh(TOA)/MG70	0.37	81	0/0	13
Ru/MG70	0.59	70	0/0	17
Ru(TOA)/MG70	0.38	82	1.64/0	15
Ru(TOA)/MG70-48	0.46	58	1.89/0	14

Fig. 1. Hydrogen consumption profiles (TPR) of Rh/MG70, trace (a); Rh(TOA)/MG70 trace (b); Ru/MG70, trace (c); Ru(TOA)/MG70, trace (d); Ru(TOA)/MG70-48, trace (e) catalysts.

Interestingly, when the residual HT content was decreased, as occurs in sample Ru(TOA)/MG70-48 (trace e), an increase in reduction temperature of ruthenium oxide NPs occurs, and a "high" temperature main peak at 174 °C is evident in TPR profile.

3.4. XRPD

Phase composition of MG70 commercial HT before and after annealing was studied by powder diffraction. Fig. 2(a) shows the XRPD pattern collected on pristine MG70HT. The diffraction peaks are consistent with rhombohedral polymorph (space group R-$3m$). In Fig. 2(b) the Rietveld refinement related to MG70 sample annealed overnight is shown as an example. All the peaks in the patterns are indexed according to the following phases: $MgAl_2O_4$ (space group Fd-3m), MgO (Fm-3m) and residual HT. We did not detect any diffraction signals belonging to supported metals. The same pattern indexing holds for XRPD related to Ru/MG70 and Ru(TOA)/MG70 samples. In Table 2, selected structural parameters together with phase fractions estimated by Rietveld method obtained for all samples are listed.

The presence of MgO and spinel-type phases are in agreement with previous study on annealing of HT at 900 °C [59]. All the catalysts obtained from MG70 annealed overnight show the same phase composition providing evidence that the different preparative approaches do not affect the composition of the support. Conversely, the annealing time strongly affects the phase composition, in particular the MgO and residual HT percentages: increasing time results in a lower amount of residual HT.

3.5. CO-DRIFTS

The presence of isolated Rh^{n+} and Ru^{n+} sites, the surface properties of metals NPs (exposed facets, corners, etc.) and their defectivity were investigated by DRIFT spectra of adsorbed CO reported in Fig. 3.

The CO-DRIFT spectra of Ru and Rh samples exposed to pure CO flow and then briefly purged in He flow, reported in Fig. 3,

showed typical features of CO linearly adsorbed on zero-valent metal nanoparticles in the wavelengths range 2100–1950 cm^{-1} and on isolated Rh^{n+} and Ru^{n+} sites. Rh samples also showed the presence of bands ascribable to bridged CO, located around 1830 cm^{-1}. Upon CO adsorption carbonates and hydrogenocarbonates absorption bands appear at 1600–1400 cm^{-1} (not shown) [60]. The convoluted bands located at 2100–1950 cm^{-1} were analyzed by a fitting procedure, the complete list of selected parameters of the resulting bands (location, height, width, area) being reported in Table 3.

The band assigned to linearly adsorbed CO on Rh^0 species (2060 cm^{-1}) appeared with about the same intensity in both the spectra of the Rh catalysts [61]. The formation of dicarbonyl species on oxidized Rh sites, that is Rh^I-(CO)$_2$, can be deduced in both the spectra by the presence of three bands related to the symmetric (2095 cm^{-1}) and antisymmetric (2041 cm^{-1}) stretching modes [62]. The intensity of these bands was found to be higher for Rh(TOA)/MG70. The broad bands centered around 1820, 1645, 1520 and 1410 cm^{-1} (not shown) can be ascribed to the presence of carbonates and hydrogenocarbonates.

Both Ru/MG70 and Ru(TOA)/MG70 samples showed bands corresponding to CO species linearly adsorbed on metallic Ru NPs, located at 2033–2035 cm^{-1}, closely resembling those found in Ru/Al$_2$O$_3$ catalyst at 2030 cm^{-1} [63]. On the other hand, CO adsorbed on highly reactive Ru^0 sites (very small Ru clusters or atoms dispersed on the support) was also detected at 1998–2001 cm^{-1}. The latter bands can be alternatively assigned also to Ru^{n+} dicarbonyl species. This assignment is also confirmed by the presence of tricarbonyl species, Ru^{n+}-(CO)$_3$, detectable at 2135 and 2069–2073 cm^{-1} [57]. These Ru species can result from the oxidative rupture of small Ru NPs [64] by a mechanism similar to the well known one occurring for Rh [62]. Only the band assigned to the dicarbonyl species had the same intensity in both the samples, in fact in Ru(TOA)/MG70 the intensity of the band related to Ru^0-(CO) species was higher and the bands of Ru^{n+}-(CO)$_3$
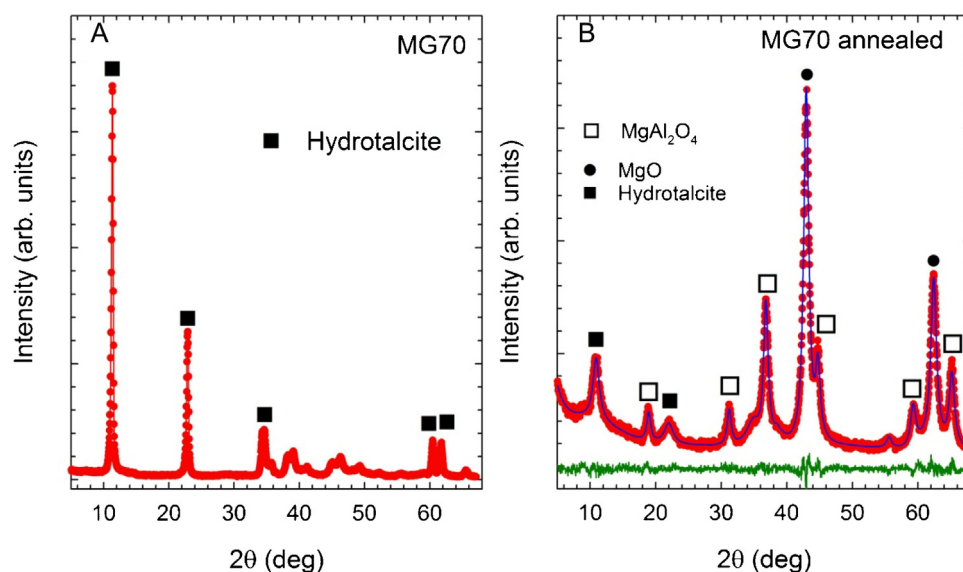
Fig. 2. (a) X-ray powder diffraction pattern of MG70 before annealing. The indexing is related to main peaks of HT phase. (b) Measured (dots), calculated (line) powder diffraction patterns and residuals (bottom line) for MG70 after annealing. Markers indicate the peaks related to identified phases.

Table 2
Selected Rietveld refinement results for annealed MG70, MG70-48, Ru/MG70 and Ru(TOA)/MG70.

|	MG70	MG70-48	Ru/MG70	Ru(TOA)/MG70
Phase 1—MgAl$_2$O$_4$				
a (Å)	8.105(1)	8.099(1)	8.095(1)	8.097(8)
V (Å^3)	532.5(2)	531.9(2)	530.5(2)	531.1(2)
Phase fraction (%)	32.61	34.1	33.72	32.60
Phase 2—MgO				
a (Å)	4.2090(6)	4.2099(5)	4.2051(6)	4.2086(5)
V (Å^3)	74.57(3)	74.62(3)	74.36(3)	74.54(2)
Phase fraction (%)	52.74	59.3	51.53	52.31
Phase 3—Hydrotalcite				
a (Å)	3.053(2)	3.054(3)	3.058(1)	3.033(8)
c (Å)	23.78(2)	23.26(4)	24.04(1)	24.18(3)
V (Å^3)	191.9(2)	187.9(3)	194.7(2)	192.7(3)
Phase fraction (%)	14.65	6.3	14.75	15.09
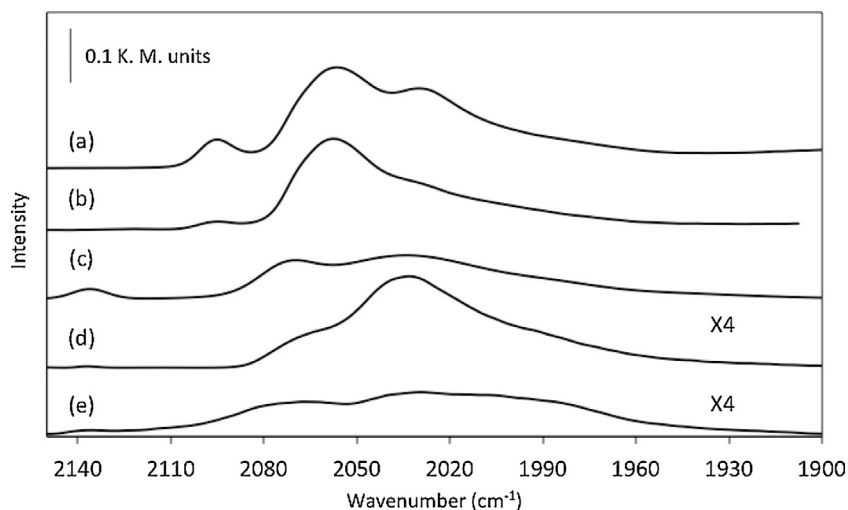
Fig. 3. CO-DRIFT spectra of Rh(TOA)/MG70, trace (a); Rh/MG70, trace (b); Ru(TOA)/MG70-48, trace (c); Ru(TOA)/MG70, trace (d); Ru/MG70, trace (e) catalysts.

Table 3
Most significant CO infrared absorption bands resulting from CO-DRIFT spectra deconvolution, with their assignment.

Sample	Center (cm^{-1})	Height (K.M. units)	Area (ratio)	Assignment/[61,63]
Rh/MG70	2095	0.013	0.16 (0.05)	sym-Rh^I-(CO)$_2$
	2060	0.135	3.25 (1.00)	Rh^0-CO
	2040	0.065	2.52 (0.77)	as-Rh^I-(CO)$_2$
Rh(TOA)/MG70	2095	0.048	0.67 (0.15)	sym-Rh^I-(CO)$_2$
	2059	0.156	4.38 (1.00)	Rh^0-CO
	2030	0.082	2.51 (0.57)	as-Rh^I-(CO)$_2$
Ru/MG70	2071	0.014	0.63 (0.46)	Ru^{n+}-(CO)$_3$
	2033	0.084	0.27 (0.20)	Ru^0-CO
	2001	0.018	1.37 (1.00)	Ru^{0*}-CO/Ru^{n+}-(CO)$_3$
Ru(TOA)/MG70	2069	0.009	0.15 (0.10)	Ru^{n+}-(CO)$_3$
	2035	0.036	1.48 (1.00)	Ru^0-CO
	1998	0.017	1.37 (0.93)	Ru^{0*}-CO/Ru^{n+}-(CO)$_2$
Ru(TOA)/MG70-48	2073	0.043	0.94 (0.18)	Ru^{n+}-(CO)$_3$
	2034	0.081	5.24 (1.00)	Ru^0-CO
	1987	0.015	0.58 (0.11)	Ru^{0*}-CO/Ru^{n+}-(CO)$_2$

species were weaker. Conversely, the band assigned to linearly adsorbed CO on Ru^{n+} species at 2114 cm^{-1} and to bridged CO species, that is Ru$_2$-(CO), at 1925 cm^{-1}, appeared only in the spectrum of Ru/MG70. A similar pattern was reported by some of us [65] for Ru/MG70 catalysts obtained by CVD of Ru(TMHD)$_3$ (TMHD = 2,2,6,6-tetramethyl-3,5-heptanedionate). It is worth noting that only bands located at 2130, 2070, and 2000 cm^{-1} were stable upon prolonged He outgassing, while 2045 cm^{-1} disappeared.

3.6. Catalytic performances

Rh based catalysts show stable and high performances irrespective of metal deposition method (see Fig. 4A), with carbon conversion values comprised between 90 and 100% and H$_2$ yield ranging from 65 to 70%. Conversely, Ru based catalysts performances strongly depend on the preparation method: Ru/MG70 activity decreases rapidly reaching, at 20 h t.o.s., 60% of C conversion and 40% of H$_2$ yield values, while Ru(TOA)/MG70 shows high performances, comparable with the reference Rh based systems (see Fig. 4B). These different behaviors could be mainly ascribed to coke deposition and/or NPs sintering phenomena, as discussed in Sections 3.3 and 3.4.

Selectivities to carbon containing products (i.e., CO, CO$_2$ and CH$_4$) are shown in Fig. 5 and generally remains stable along t.o.s., with Ru based catalysts showing a slightly higher selectivity to CO$_2$ and CH$_4$ if compared to Rh based ones. Finally, Ru(TOA)/MG70-48 sample shows good starting performances (H$_2$ yield = 58% and C conversion = 95%), but it deactivates at longer time on stream (H$_2$ yield = 55% and C conversion = 86%).

Ru(TOA) catalysts were further tested under more demanding reaction conditions, as shown in Fig. 6, doubling WHSV up to 12 h^{-1} and their good performances were substantially confirmed, C conversion being almost complete, while observing only a 7% decrease in H$_2$ yield, and even minor variations in selectivity to CO, CO$_2$ and CH$_4$. On the contrary, the decrease of T_R down to 600 °C results in a decrease of both C conversion and H$_2$ yield that reach 83.7 and 47.8% values, respectively. On the other hand, CO$_2$ and CH$_4$ selectivities increase to 76.9 and 5.3%, respectively, while CO selectivity decreases to 17.8%.

Specific activity, expressed as TOF, of the different Rh and Ru catalysts is reported in Table 4.

Ru(TOA)/MG70 and Rh(TOA)/MG70 showed comparable specific activities (ranging 2100–2500 h^{-1}), stable during reaction, and higher than those measured for Rh/MG70 and Ru/MG70. The latter shows deactivation, passing from a TOF of 1500 to 1170 h^{-1}. Ru(TOA)/MG70-48 tested at double WHSV (i.e., 12 h^{-1} vs 6 h^{-1})

Table 4
Specific activities at 5 and 20 h of t.o.s. for Rh and Ru based catalysts at T_R = 700 °C, WHSV = 6 h^{-1}.

Sample	Dispersion (%)	t.o.s. (h)	TOF^a (h^{-1})
Rh/MG70	39	5	1690
		20	1740
Rh(TOA)/MG70	42	5	2140
		20	2250
Ru/MG70	31	5	1500
		20	1170
Ru(TOA)/MG70	38	5	2350
		20	2470
Ru(TOA)/MG70-48	39	5	3770^b
		20	3420^b

[a] TOF based on C conversion to gaseous products (CO$_2$, CO, CH$_4$).
[b] T_R = 700 °C, WHSV = 12 h^{-1}.

Table 5
Coke integral deposition rates on Rh and Ru catalysts. Coke amount measured on used catalysts after 20 h t.o.s., T_R = 700 °C, WHSV = 6 h^{-1}.

Sample	Coke (mg$_{coke}$ g$_{cat}$$^{-1}$ h^{-1})
Rh/MG70	3.4
Rh(TOA)/MG70	1.9
Ru/MG70	4.9
Ru(TOA)/MG70	2.0
Ru(TOA)/MG70^a	3.1
Ru(TOA)/MG70^b	2.6
Ru(TOA)/MG70-48^a	3.3

[a] T_R = 700 °C, WHSV = 12 h^{-1}.
[b] T_R = 600 °C, WHSV = 12 h^{-1}. (The apparent mismatch between the TGA profiles in Fig. 7 and the values reported in Table 5 is due to the residual presence of quartz beads used as fillers to ensure a better thermal contact of the catalyst with the thermocouple during the catalytic tests.)

revealed good activity even if some deactivation occurred at 20 h t.o.s.

3.7. Coke characterization (TGA)

TGA of Ru and Rh based catalysts after catalytic runs (Fig. 7) revealed the occurrence of a mass loss in the range 350–550 °C, due to the combustion of coke deposited on the catalysts. Lowest coke deposition occurred on TOA derived systems (Table 5), regardless of metal (i.e., 2.0 and 1.9 mg$_{coke}$ g$_{cat}$$^{-1}$ h^{-1} for Ru(TOA) and Rh(TOA) respectively). Conversely, the highest coke amount was found to be deposited on Ru/MG70 sample. Notwithstanding, the increase of WHSV results only in a slight increase of catalysts coking.
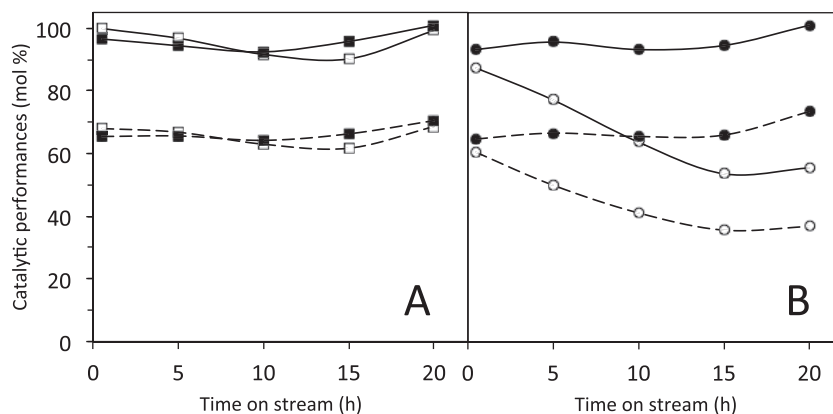
Fig. 4. Catalytic performances measured as H_2 yield (dashed line) and carbon conversion (continuos line) of Rh/MG70 (empty squares); Rh(TOA)/MG70 (full squares) catalysts (A) and of Ru/MG70 (empty circles); Ru(TOA)/MG70 (full circles) (B) catalysts, as measured at $T_R = 700\,°C$, WHSV = 6 h^{-1}, S/C = 3.
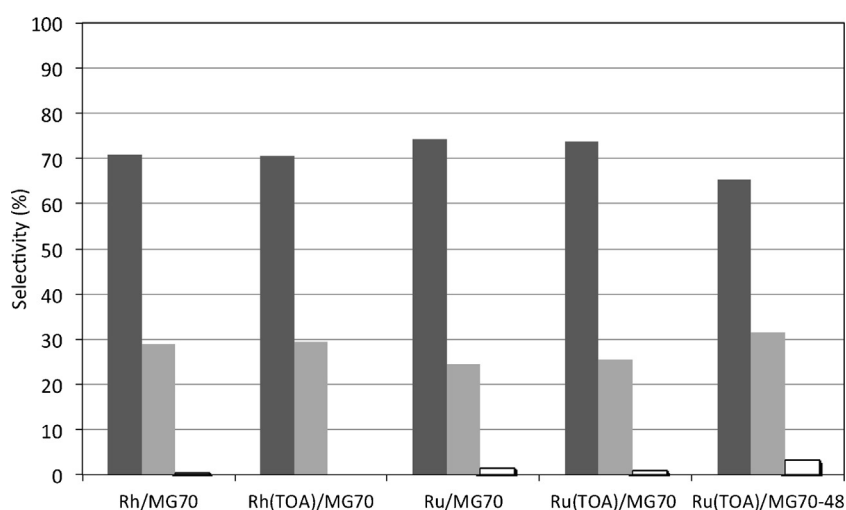

Fig. 5. Selectivity to CO_2 (dark gray bar), CO (light gray bar), and CH_4 (black bordered) of Rh; Rh(TOA); Ru; Ru(TOA)/MG70 catalysts, as measured at 20 h t.o.s., $T_R = 700\,°C$, WHSV = 6 h^{-1}, S/C = 3, and Ru(TOA)/MG70-48 at WHSV = 12 h^{-1}.
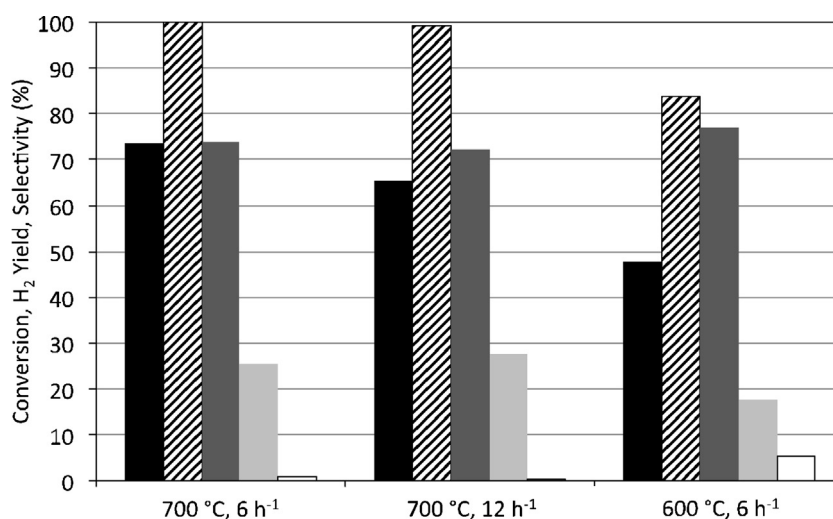
Fig. 6. Catalytic performances of Ru(TOA)/MG70 catalyst (H_2 yield, black bar; C conversion, dashed bar; CO_2 sel., dark grey bar; CO sel., light grey bar; CH_4 sel., white bordered bar) as measured at S/C = 3 and t.o.s. = 20 h under different reaction conditions: $T_R = 700\,°C$, WHSV = 6 h^{-1}; $T_R = 700\,°C$, WHSV = 12 h^{-1}, $T_R = 600\,°C$, WHSV = 6 h^{-1}.

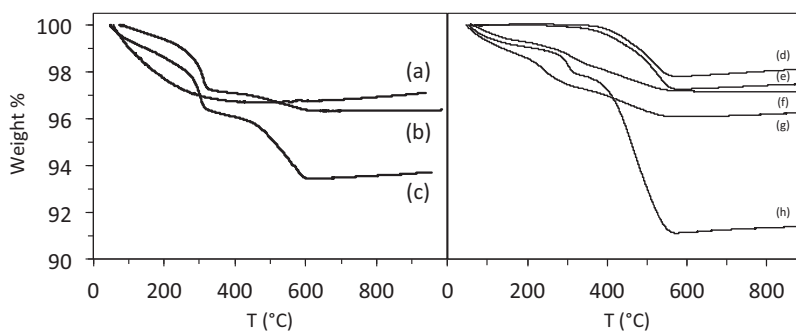**Fig. 7.** TGA profiles of bare MG70, trace (a); Rh(TOA)/MG70, trace (b); Rh/MG70, trace (c); Ru(TOA)/MG70 (T_R = 600 °C), trace (d); Ru(TOA)/MG70-48, trace (e); Ru(TOA)/MG70 (WHSV = 12 h^{-1}), trace (f); Ru(TOA)/MG70 (WHSV = 6 h^{-1}), trace (g); Ru/MG70, trace (h) catalysts.
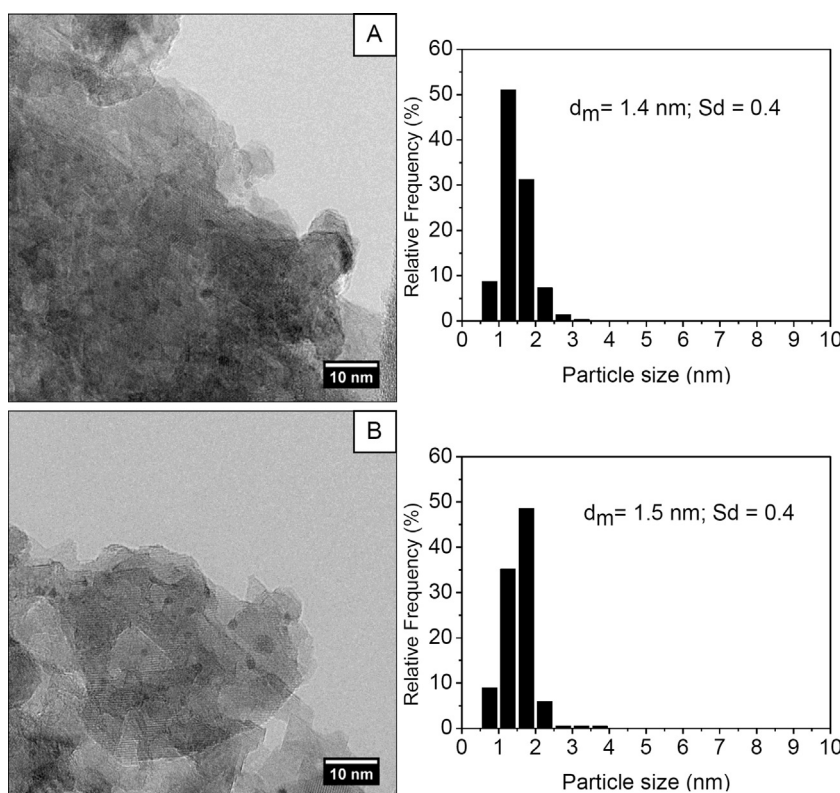

Fig. 8. HRTEM micrographs and particle size distributions of freshly prepared Rh(TOA)/MG70 (A) and Rh/MG70 (B).

3.8. Catalysts stability (HRTEM, XRPD)

HRTEM micrographs were collected on fresh catalysts prior to catalytic run and on the used ones after 20 h of catalytic experiments.

Rh supported Mg(Al)O samples (Fig. 8A and B) prepared following the two different synthetic approaches present metal particles highly dispersed on the solid support with very similar sizes. In both samples a narrow particle size distribution, mainly ranging 0.5–2.5 nm, with a comparable mean diameter (1.4 nm and 1.5 nm for Rh(TOA)/MG70 and Rh/MG70, respectively) was observed. Conversely, HRTEM micrographs of the Ru samples (Fig. 9A–C) revealed for SCMNs deposition-derived Ru catalysts (both Ru(TOA)/MG70 and Ru(TOA)/MG70-48) smaller metal particles' sizes with a narrower size distribution when compared to traditionally impregnated ones. Ru NPs in Ru(TOA)/MG70 and Ru(TOA)/MG70-48 have a mean size of 1.6 and 1.5 nm, respectively with a s.d. of 0.5 nm, while in Ru/MG70 Ru NPs are larger (mean size = 2.6 nm) and the distribution is slightly broader (s.d. = 1.2 nm). Interestingly, the comparison between the HRTEM analysis of Rh(TOA) and Ru(TOA) soluble nanoparticles (Figs. S1 and S2) with the corresponding deriving supported systems samples, evidenced that no aggregation of the metal particles occurred in the deposition step.

Once employed in SR reaction Rh catalysts revealed some sintering, more evident in impregnated sample, with an increase of mean particle size from 1.4 to 1.8 nm and from 1.5 to 2.0 nm for Rh(TOA)/MG70 and Rh/MG70, respectively; while size distribution continued to be sharp, with s.d. = 0.4 (Fig. 10A and B).

On the other hand, Ru catalysts, supported on MG70, showed only a small increase in mean particle size: from 1.6 to 1.8 nm and from 2.6 to 2.7 nm for Ru(TOA)/MG70 and Ru/MG70, respectively, but size distribution of the latter was still broad and a very low amount of larger particles ranging 10–15 nm in diameter, was also detected in the used sample (Fig. 11A and B).
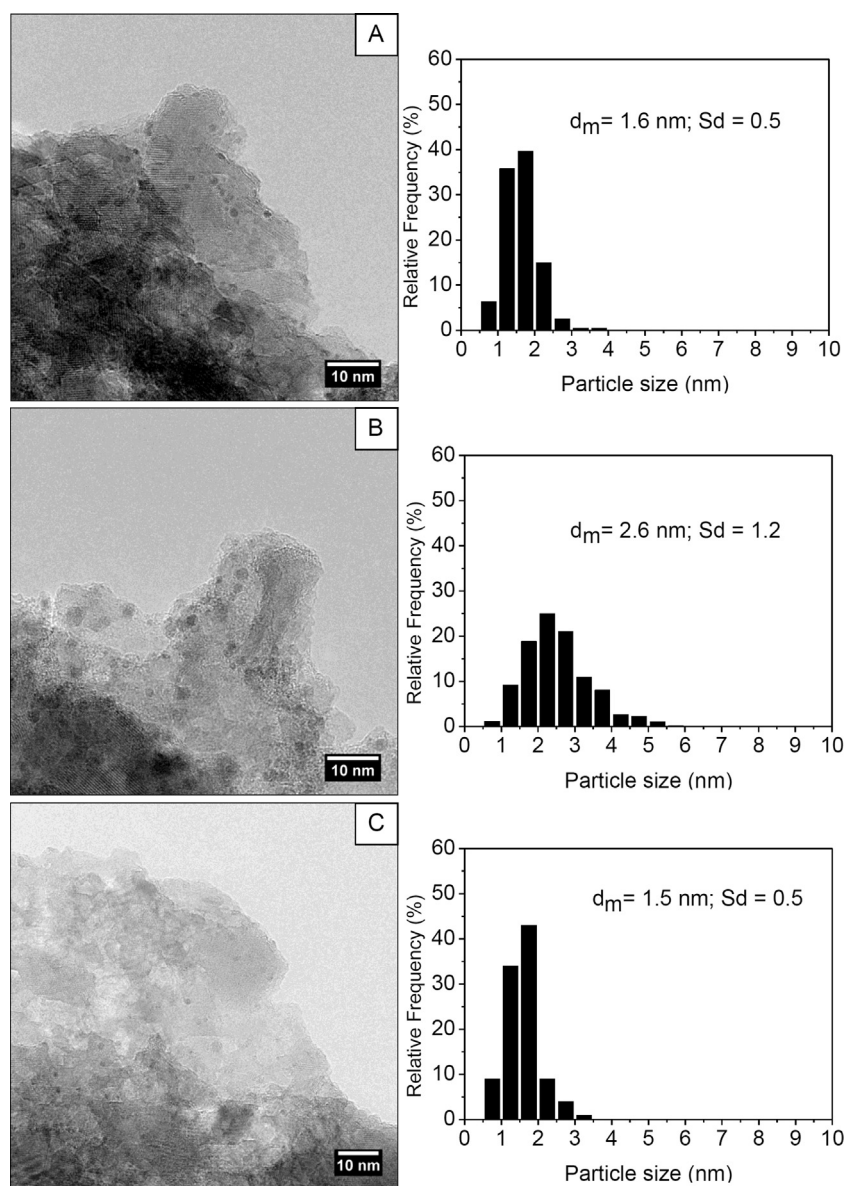
Fig. 9. HRTEM micrographs and particle size distributions of freshly prepared Ru(TOA)/MG70 (A), Ru/MG70 (B) and Ru(TOA)/MG70-48 (C).
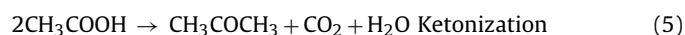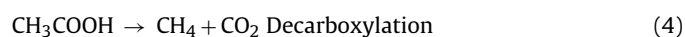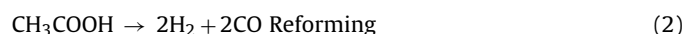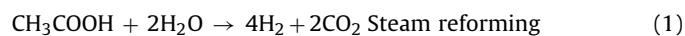
Conversely, Ru(TOA)/MG70-48 catalyst shows a different behavior: after catalytic test NPs size increases from 1.5 (Fig. 9C) to 2.6 nm (Fig. 11C), such sintering can be related to the lower amount of residual HT phase in MG70-48 support.

Actually, the analysis of Ru(TOA)/MG70 and Ru(TOA)/MG70-48 structural phases after the catalytic tests was studied by XRPD. A low angle magnification of the Rietveld refinements related to the samples is shown in Fig. 12. Diffraction signals related to HT phase were not detected in Ru(TOA)/MG70-48 whereas Ru(TOA)/MG70 is composed by MgO 54.42%, MgAl$_2$O$_4$ 30.57% and HT 15.01%. MgO and MgAl$_2$O$_4$ phase fractions are 70.41% and 29.59% in Ru(TOA)/MG70-48 sample. Again the diffraction scattering from the supported metal was not detected in both the samples.

4. Discussion

Catalytic performances of Rh, Rh(TOA) and Ru(TOA) catalysts are comparable with those reported for similar Ru-based systems [14] and also for more diffused Ni-based systems [10,66–68], under comparable reaction conditions.

Steam reforming (Eq. (1)) and reforming (Eq. (2)) reactions take place leading to hydrogen, carbon dioxide and carbon monoxide as main products. On the other hand, at temperature above 400–500 °C the ketonization reaction (Eq. (5)) extent is almost zero. Noteworthy, the H$_2$ yield close to 65% and the CO$_2$ selectivity around 70%, at total C conversion, are a direct proof of the importance of reforming reaction for such low S/C ratios. The higher WGS activity of Ru can account for the slightly higher CO$_2$/CO ratio: 3.0 and 2.5 for Ru and Rh systems, respectively.

$$CH_3COOH + 2H_2O \rightarrow 4H_2 + 2CO_2 \text{ Steam reforming} \tag{1}$$

$$CH_3COOH \rightarrow 2H_2 + 2CO \text{ Reforming} \tag{2}$$

$$CO + H_2O \rightarrow CO_2 + H_2 \text{ WGS} \tag{3}$$

$$CH_3COOH \rightarrow CH_4 + CO_2 \text{ Decarboxylation} \tag{4}$$

$$2CH_3COOH \rightarrow CH_3COCH_3 + CO_2 + H_2O \text{ Ketonization} \tag{5}$$

$$CO + 3H_2 \rightarrow CH_4 + H_2O \text{ CO methanation} \tag{6}$$

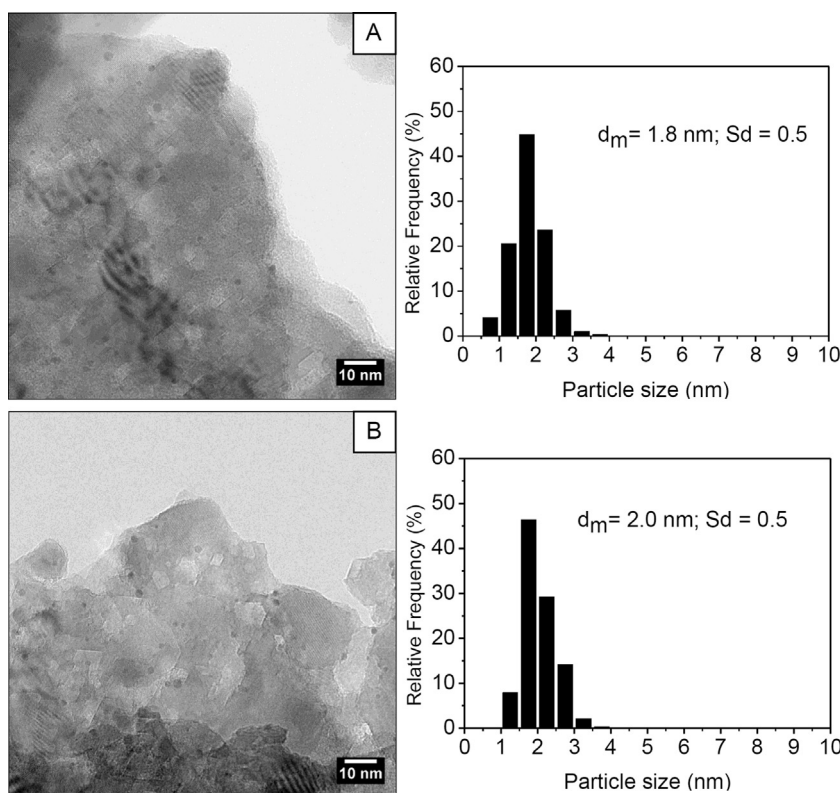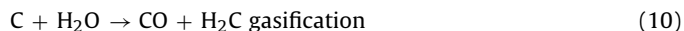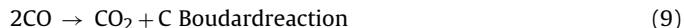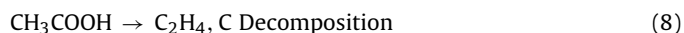$$CO_2 + 4H_2 \rightarrow CH_4 + 2H_2O \text{ CO}_2 \text{ methanation} \tag{7}$$

Fig. 10. HRTEM micrographs and particle size distributions of Rh(TOA)/MG70 (A) and Rh/MG70 (B) after catalysis (20 h).

$$CH_3COOH \rightarrow C_2H_4, C \text{ Decomposition} \qquad (8)$$

$$2CO \rightarrow CO_2 + C \text{ Boudardreaction} \qquad (9)$$

$$C + H_2O \rightarrow CO + H_2C \text{ gasification} \qquad (10)$$

The observed small decrease in hydrogen yield and in CO_2 selectivity as a consequence of the space velocity (WHSV) increase from 6 to $12\,h^{-1}$ for Ru(TOA) can be accounted by a decrease of steam reforming and WGS activity. Conversely, the decrease in reaction temperature from 700 to 600 °C results in an appreciable decrease in the reforming activity, more evident for reforming reaction, while WGS activity is promoted by the lower temperature and some decarboxylation (Eq. (4)), leading to a 5.3% of methane selectivity. Methanation reactions cannot be excluded and could provide methane in CO_2, CO, H_2 rich environment (Eqs. (6) and (7)) [60].

Coke detected in all the catalysts has mainly aromatic (graphitic) nature since its oxidation occurs at temperatures between 450 and 600 °C. Interestingly, filamentous carbon was not detected due to the low C solubility in Rh and Ru small nanoparticles. Its formation can occur both by acetic acid decomposition (Eq. (8)) and Boudard reaction (Eq. (9)) and is generally quite low for all the catalysts under all the investigated conditions. This behavior is in agreement with the well known properties of both $MgAl_2O_4$ [14] and MgO [60] to promote H_2O adsorption and OH and O spillover from support to metal thus promoting C gasification (Eq. (10)) even at low S/C ratios.

Notably, it is worth to note that coke amount is not dependent on the nature of the metal, but on the preparation method, as SCMNPs catalysts show lower C deposition rates if compared with traditionally impregnated systems.

Finally, all the catalysts show a good stability except for Ru/MG70 system, which suffers an evident deactivation with performances readily decreasing yet at the beginning of the reaction. This behavior can be accounted mainly by the observed increase in coke amount since Ru NPs are stable against sintering as revealed by TGA and HRTEM measurements. Conversely, Ru(TOA)/MG70-48 showed a similar deactivation, even in less extent, that could be ascribed mainly to Ru NPs sintering (coke deposition is comparable to the one of stable catalysts), as evidenced by HRTEM micrographs and size distribution data.

Actually, coke deposition and nanoparticles sintering are the most important deactivation causes in steam reforming catalysts. Coke is mainly deposited by surface reactions on acidic sites of support oxides [65] or by decomposition occurring at defects on metal NPs [69], and nanoparticles sintering is a more complex phenomenon depending on several parameters. Some of these parameters can be related to the metal, such as its nature (i.e., its melting point temperature), reducibility, ionic radius/charge ratio for the inclusion in support lattice. Others are ascribable to the support, such as nature of the lattice, ease of ions substitution and of formation of mixed oxides with metal ions, metal-support interactions, etc.

Considering the typical steam reforming reaction conditions, namely, high temperature, presence of steam, oxidative and reductive conditions, presence of species able to promote metals oxidative disgregation such as CO, the ideal catalysts should possess some peculiar features: low concentration of surface acidic and basic sites, ability to interact with supported metal NPs (to limit sintering) but low tendency to form mixed oxides and to host and stabilize isolated oxidized metal sites.

As far as metal NPs stability against sintering is concerned, usually Ru NPs show high stability that can be ascribed to the properties of Mg(Al)O spinel phase [37,65] and it is in apparent contrast with recent report by Li et al. [70] which ascribes the low stability to the lattice mismatch and to the lack of strong electronic attractions between the spinel (1 1 1) surface oxygen and metals/metal oxides. However, in our case Ru NPs are much more smaller even from the beginning of synthesis and our support consists not only of $MgAl_2O_4$ phase but contains also MgO and unconverted HT that
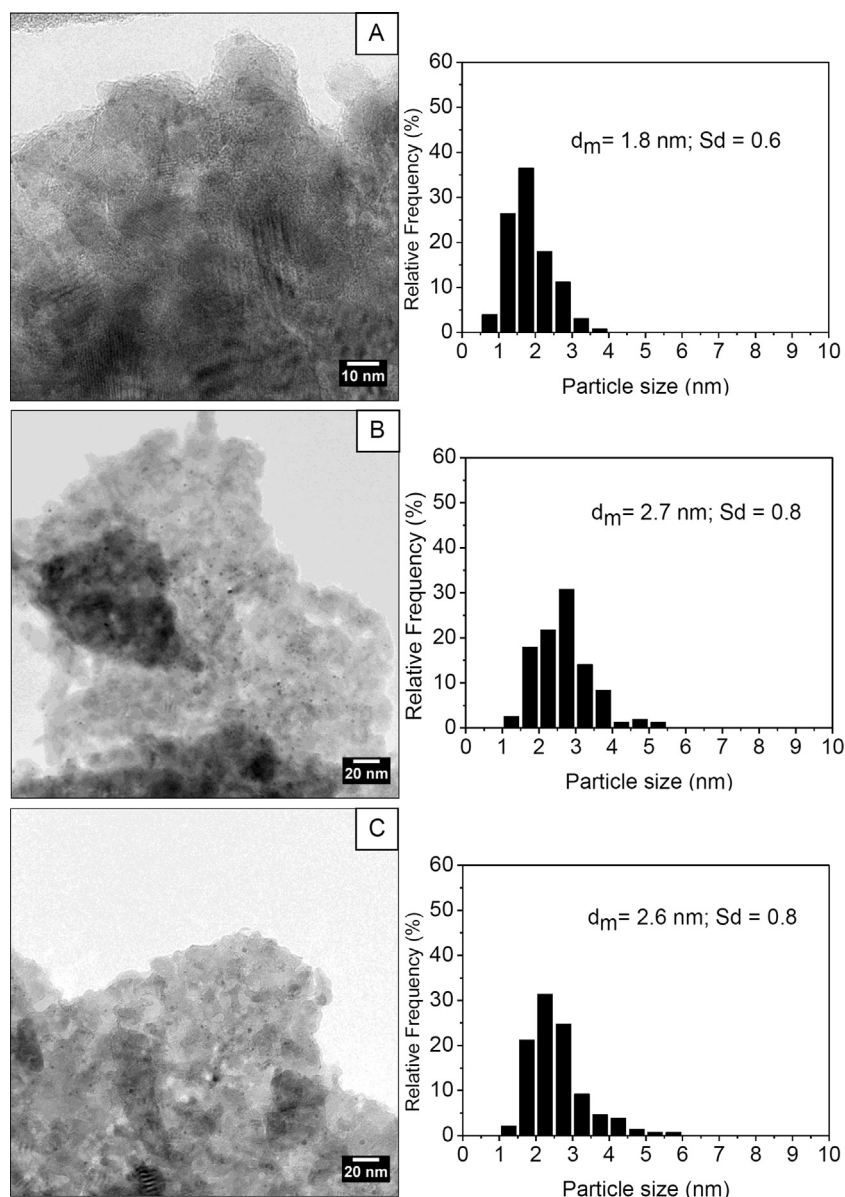
Fig. 11. HRTEM micrographs and particle size distributions of Ru(TOA)/MG70 (A), Ru/MG70 (B) and Ru(TOA)/MG70-48 (C) after catalysis (20 h).

can play a significant role in stabilizing Ru NPs. Metal NPs can interact with each one of these phases with different adhesion energies [71] that also depend on the metal and the size of the NPs.

Assuming a significant fraction of residual HT located preferentially on the external surface of support grains, it is reasonable that metal NPs have major interaction with HT itself rather than with $MgAl_2O_4$ and MgO.

The contribution of residual HT phase in stabilizing Ru NPs was further confirmed by the occurrence of some sintering only in Ru(TOA)/MG70-48, after catalytic tests Ru NPs mean size increased from 1.5 to 2.6 nm, while Ru(TOA)/MG70 showed only a negligible increase from 1.6 to 1.8 nm. This behavior is reflected also by the catalytic performances of Ru(TOA)/MG70-48 sample, which shows a decrease of conversion, hydrogen yield and CO_2 selectivity yet after 5 h of t.o.s. These evidences are also in agreement with XRPD data showing a residual amount of HT, after catalytic runs, only in Ru(TOA)/MG70, while it is undetectable in Ru(TOA)/MG70-48 sample.

As far as coke deposition concerns, Py-FTIR characterization clearly showed that all the catalysts present similar, low surface acidity, mainly consisting in Lewis acid sites. This evidence is consistent with previous reports on Mg(Al)O mixed oxide supports and LAS is mainly due to Mg^{2+} c.u.s. sites and octahedral and tetrahedral Al^{3+} sites present on MG70 surface. Moreover, since LAS concentrations measured on metal loaded MG70 are close to the ones of the bare support, the formation of acidic sites induced by small metal nanoparticles, even occurring on non acid supports [72], is not operative in our samples, even for very small Rh(TOA) and Ru(TOA) NPs.

Consequently, the differences in coke integral deposition rates, which follow the order Ru/MG70 > Rh/MG70 > Rh(TOA)/MG70 ∼ Ru(TOA)/MG70, found onto our catalysts (measured under the same reaction conditions) cannot be related only to surface reactions occurring on surface acid sites.

The absence or at least the significant decrease of defects (i.e., steps, kinks, etc.) of supported metal nanoparticles exerts relevant effects on their catalytic performances, well formed Rh NPs were reported to catalyze more selectively C-reforming rather than C-forming reactions in CH_4–CPO, thus avoiding coke accumulation
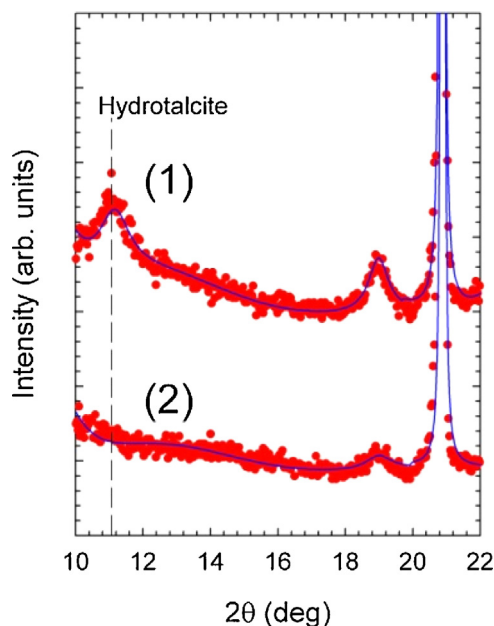
Fig. 12. Measured (dots), calculated (line) powder diffraction patterns for (1) Ru(TOA)/MG70 and (2) Ru(TOA)/MG70-48 MG70 after catalytic tests. Vertical dashed line marks the main diffraction peak related to HT phase.

and improving activity and selectivity [62,73,74]. Similar evidences were also reported for Ag/Ni catalysts where coordinatively unsaturated sites/step sites act as nucleation centers promoting the growth of filamentous carbon [75].

A perusal of our characterization data clearly shows how ruthenium nanoparticles present in Ru(TOA) catalysts are more well formed with respect to Ru impregnated ones.

These data recall the behavior of Rh based CH_4–CPO catalysts previously reported by some of us [62,74]. In that case catalysts obtained by conventional nitrates impregnation showed the presence of isolated oxidized sites and the resulting low Rh(0)/Rh(I) ratio, that is a clear indication of defective and not-well formed Rh NPs. Conversely, Rh NPs obtained by a peculiar multi-step OM-CVD showed an opposite behavior, ascribed to the presence of well formed, less defective metal nanoparticles. Since Rh(I)(CO)$_2$ sites derive by the oxidative disgregation reaction, from Rh clusters, rafts and defective particles (Eq. (11)), a low Rh(0)/Rh(I) ratio indicates an higher amounts of defective rhodium nanoparticles with respect to "stable" ones [76].

$$1/nRh^0{}_n + 2CO + xOH^- \rightarrow (O^{2-})_xRh^I(CO)_2 + 0.5xH_2 \quad x = 1\text{--}2 \quad (11)$$
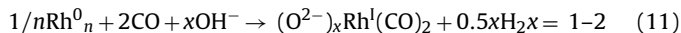
On the other hand, CO-DRIFTS data, recorded on reduced catalysts, account for the presence in Ru(TOA), Rh(TOA), and Rh/MG70 of a higher fraction of CO linearly bonded to metallic NPs with respect to Ru/MG70. More in detail, in the latter sample a higher amount of di- and tri-carbonyls ruthenium species (Ru^{n+}-(CO)$_m$ with $m = 2, 3$) were detected that can result from small ruthenium clusters formed by CO disgregation of defects-rich ruthenium nanoparticles.

The easiest formation of isolated oxidized surface carbonyls, such as Rh(I)(CO)$_2$ and Ru^{n+}-(CO)$_x$ ($x = 2, 3$), occurring on impregnated Rh and Ru MG70 catalysts, cannot be simply ascribed to the high number of surface metal atoms in low coordination, which are the most reactive in the reaction with CO leading to Rh(I) and Ru^{n+} di- or tri-carbonyls, usually present in low dimension metal NPs (i.e., the number of coordinatively unsaturated surface atoms on corners and edges is expected to increase as the size of metal NPs decreases) as already reported by some of us [43,45].

TPR data further confirm this interpretation: reduction peaks occurring in our traditionally impregnated Ru samples are comparable to the low temperatures peaks reported for co-precipitated samples [39,58] which show well-dispersed RuO$_x$ and bulk RuO$_2$ reduction peaks around 200–250 °C. Notably, strongly interacting species that usually are reduced at higher temperatures, for instance at 400 °C for alumina supported Ru, are totally absent in our samples.

SMNCPs derived systems show even lower reduction temperatures thus confirming the very low presence of species interacting with support, that, upon reduction, can afford Ru$^+$ sites or small clusters in close proximity of metallic NPs and, finally, defective metal NPs.

5. Conclusions

Ru and Rh SCMNPs were easily prepared by H$_2$-reduction of the corresponding metal chlorides in presence of trialkylamines. Low loaded metal catalysts were obtained by SCMNPs deposition on Mg–Al mixed oxides supports. Ru catalysts showed good performances, as activity and selectivity are concerned, (73% H$_2$ yield, 74% CO$_2$ selectivity and total C conversion at 700 °C, WHSV = 6 h^{-1}, S/C = 3) in the steam reforming of acetic acid, fully comparable with those obtained with Rh-based systems. Ru SCMNs derived catalysts showed also high stability under reaction conditions (100% C conv.; 65% H$_2$ yield, 72% CO$_2$ sel., after 20 h t.o.s. at 700 °C, WHSV = 12 h^{-1}, S/C = 3) superior to that of traditionally impregnated catalysts. This behavior was ascribed to the presence of well formed, crystalline metal nanoparticles, with uniform size distribution, able to keep coke deposition rate as low as 2.0 mg$_{coke}$ g$_{cat}$$^{-1}$ h^{-1}. Moreover, their stability against sintering was improved by the presence of residual unconverted hydrotalcite, which enhanced strong metal support interactions.

Appendix A. Supplementary data

Supplementary data associated with this article can be found, in the online version, at http://dx.doi.org/10.1016/j.apcatb.2015.08.024.

References

[1] M.A. Laguna-Bercero, J. Power Sources 203 (2012) 4–16.
[2] P. Millet, R. Ngameni, S.A. Grigoriev, N. Mbemba, F. Brisset, A. Ranjbari, C. Etievant, Int. J. Hydrogen Energy 35 (2010) 5043–5052.
[3] K. Rajeshwar, J. Appl. Electrochem. 37 (2007) 765–787.
[4] A. Gallo, T. Montini, M. Marelli, A. Minguzzi, V. Gombac, R. Psaro, P. Fornasiero, V. Dal Santo, ChemSusChem 5 (2012) 1800–1811.
[5] H. Hochrinner, Linde Technology, 2 (2011) 16–21.
[6] BTG's Biomass Gasification Expertise—Gaseous Biofuel from Biomass & Waste brochure, http://www.btgworld.com/en/references/brochures/btg-biomass-gasification-expertise-gaseous-biofuel-from-biomass-and-waste.pdf
[7] M. Staš, D. Kubička, J. Chudoba, M. Pospíšil, Energy Fuels 28 (2014) 385–402.
[8] W.N.R.W. Isahak, M.W.M. Hisham, M.A. Yarmo, T.-y.Y. Hin, Renew. Sustain. Energy Rev. 16 (2012) 5910–5923.
[9] C. Rioche, S. Kulkarni, F.C. Meunier, J.P. Breen, R. Burch, Appl. Catal. B: Environ. 61 (2005) 130–139.
[10] E.C. Vagia, A.A. Lemonidou, Appl. Catal. A: Gen. 351 (2008) 111–121.
[11] A.A. Lemonidou, E.C. Vagia, J.A. Lercher, ACS Catal. 3 (2013) 1919–1928.
[12] E.C. Vagia, A.A. Lemonidou, J. Catal. 269 (2010) 388–396.
[13] A.C. Basagiannis, X.E. Verykios, Int. J. Hydrogen Energy 32 (2007) 3343–3355.

[14] A.C. Basagiannis, X.E. Verykios, Appl. Catal. B: Environ. 82 (2008) 77–88.
[15] A.C. Basagiannis, X.E. Verykios, Catal. Today 127 (2007) 256–264.
[16] T. Yamazaki, K. Matsuki, J. Jpn. Pet. Inst. 49 (2006) 246–255.
[17] C.M. Jeong, G.W. Park, J.-d.-r. Choi, J.W. Kang, S.M. Kim, W.-H. Lee, S.I. Woo, H.N. Chang, Int. J. Hydrogen Energy 36 (2011) 7505–7515.
[18] T.M.C. Hoang, B. Geerdink, B.J.M. Sturm, L. Lefferts, K. Seshan, Appl. Catal. B: Environ. 163 (2015) 74–82.
[19] G. Garbarino, E. Finocchio, A. Lagazzo, I. Valsamakis, P. Riani, V.S. Escribano, G. Busca, Appl. Catal. B: Environ. 147 (2014) 813–826.
[20] H. Xie, Q. Yu, M. Wei, W. Duan, X. Yao, Q. Qin, Z. Zuo, Int. J. Hydrogen Energy 40 (2015) 1420–1428.
[21] F. Zhang, N. Wang, L. Yang, M. Li, L. Huang, Int. J. Hydrogen Energy 39 (2014) 18688–18694.
[22] P.G.M. Assaf, F.G.E. Nogueira, E.M. Assaf, Catal. Today 213 (2013) 2–8.
[23] K.K. Pant, P. Mohanty, S. Agarwal, A.K. Dalai, Catal. Today 207 (2013) 36–43.
[24] Y. Sekine, Y. Nakazawa, K. Oyama, T. Shimizu, S. Ogo, Appl. Catal. A: Gen. 472 (2014) 113–122.
[25] X. Hu, G. Lu, Appl. Catal. B: Environ. 99 (2010) 289–297.
[26] R.-r. Hu, C.-f. Yan, X.-x. Zheng, H. Liu, Z.-y. Zhou, Int. J. Hydrogen Energy 38 (2013) 6033–6038.
[27] X. Hu, L. Zhang, G. Lu, Appl. Catal. A: Gen. 427–428 (2012) 49–57.
[28] P.N. Kechagiopoulos, S.S. Voutetakis, A.A. Lemonidou, I.A. Vasalos, Energy Fuels 20 (2006) 2155–2163.
[29] X. Hu, G. Lu, Appl. Catal. B: Environ. 88 (2009) 376–385.
[30] F. Bimbela, D. Chen, J. Ruiz, L. García, J. Arauzo, Appl. Catal. B: Environ. 119–120 (2012) 1–12.
[31] K. Takehira, T. Ohi, T. Miyata, M. Shiraga, T. Sano, Top. Catal. 42–43 (2007) 471–474.
[32] A. Fonseca Lucrédio, E. Moreira Assaf, J. Power Sources 159 (2006) 667–672.
[33] H.-J. Lee, Y.-S. Lim, N.-C. Park, Y.-C. Kim, Chem. Eng. J. 146 (2009) 295–301.
[34] F. Basile, G. Fornasari, V. Rosetti, F. Trifiro, A. Vaccari, Catal. Today 91–92 (2004) 293–297.
[35] S.-Y. Park, J.-H. Kim, D.-J. Moon, N.-C. Park, Y.C. Kim, J. Nanosci. Nanotechnol. 10 (2010) 3175–3179.
[36] J. Rass-Hansen, C.H. Christensen, J. Sehested, S. Helveg, J.R. Rostrup-Nielsen, S. Dahl, Green Chem. 9 (2007) 1016–1021.
[37] A. Gallo, C. Pirovano, P. Ferrini, M. Marelli, R. Psaro, S. Santangelo, G. Faggio, V. Dal Santo, Appl. Catal. B: Environ. 121–122 (2012) 40–49.
[38] C. Su, W. Wang, R. Ran, Z. Shao, M.O. Tade, S. Liu, J. Mater. Chem. A: Mater. Energy Sustain. 1 (2013) 5620–5627.
[39] A. Ballarini, P. Benito, G. Fornasari, O. Scelza, A. Vaccari, Int. J. Hydrogen Energy 38 (2013) 15128–15139.
[40] Metal Nanoclusters in Catalysis and Materials Science: The Issue of Size Control, in: B. Corain, G. Schmid, N. Toshima (Eds.), Elsevier, Amsterdam, 2008.
[41] H. Bonnemann, G. Braun, W. Brijoux, R. Brinkmann, A. Schulze Tilling, K. Seevogel, K. Siepen, J. Organomet. Chem. 520 (1996) 143–162.
[42] V.M. Frolov, Platinum Met. Rev. 40 (1996) 8–18.
[43] G. Vitulli, C. Evangelisti, P. Pertici, A.M. Caporusso, N. Panziera, P. Salvadori, M.G. Faga, C. Manfredotti, G. Martra, S. Coluccia, A. Balerna, S. Colonna, S. Mobilio, J. Organomet. Chem. 681 (2003) 37–50.
[44] G. Marconi, P. Pertici, C. Evangelisti, A.M. Caporusso, G. Vitulli, G. Capannelli, M. Hoang, T.W. Turney, J. Organomet. Chem. 689 (2004) 639–646.
[45] M.G. Faga, L. Bertinetti, C. Manfredotti, G. Martra, C. Evangelisti, P. Pertici, G. Vitulli, Stud. Surf. Sci. Catal. 155 (2005) 227–237.
[46] A. Gallo, C. Pirovano, M. Marelli, R. Psaro, V. Dal Santo, Chem. Vap. Deposition 16 (2010) 305–310.
[47] J. Kim, J. Kim, D. Lee, Appl. Catal., A: Gen. 499 (2015) 197–204.
[48] L.S. Carvalho, A.R. Martins, P. Reyes, M. Oportus, A. Albonoz, V. Vicentini, M.C. do Rangel, Catal. Today 142 (1–2) (2009) 52–60.
[49] C.A. Emeis, J. Catal. 141 (1993) 347–354.
[50] A.C. Larson, R.B. Von Dreele, General Structural Analysis System (GSAS), Los Alamos National Laboratory Report LAUR 86–748 (2004).
[51] P. Fischer, Z. Kristallogr. 144 (1977).
[52] N.G. Schmahl, G.F. Eikerling, Z. Phys. Chem. 62 (1968) 268.
[53] M. Bellotto, B. Rebours, O. Clause, J. Lynch, D. Bazin, E. Elkaim, J. Phys. Chem. 100 (1996) 8527–8534.
[54] A. Borodziński, M. Bonarowska, Langmuir 13 (1997) 5613–5620.
[55] V. Dal Santo, C. Dossi, A. Fusi, R. Psaro, C. Mondelli, S. Recchia, Talanta 66 (2005) 674–682.
[56] C. Mondelli, V. Dal Santo, A. Trovarelli, M. Boaro, A. Fusi, R. Psaro, S. Recchia, Catal. Today 113 (2006) 81–86.
[57] H.A. Prescott, Z. Li, E. Kemnitz, A. Trunschke, J. Deutsch, H. Lieske, A. Auroux, J. Catal. 234 (2005) 119–130.
[58] P. Betancourt, A. Rives, R. Hubaut, C.E. Scott, J. Goldwasser, Appl. Catal. A: Gen. 170 (1998) 307–314.
[59] F. Basile, P. Benito, G. Fornasari, F.M. Labajos, V. Rives, V. Rosetti, A. Vaccari, Stud. Surf. Sci. Catal. 162 (2006) 761–768.
[60] G. Martra, F. Arena, M. Baricco, S. Coluccia, L. Marchese, A. Parmaliana, Catal. Today 17 (1993) 449–458.
[61] F. Basile, I. Bersani, P. Del Gallo, S. Fiorilli, G. Fornasari, D. Gary, R. Mortera, B. Onida, A. Vaccari, Int. J. Spectrosc. 2011 (2011), Article ID 458089.
[62] V. Dal Santo, A. Gallo, M.M. Gatti, V. De Grandi, R. Psaro, L. Sordelli, S. Recchia, J. Mater. Chem. 19 (2009) 9030–9037.
[63] S.Y. Chin, C.T. Williams, M.D. Amiridis, J. Phys. Chem. B 110 (2006) 871–882.
[64] S. Eckle, Y. Denkwitz, R.J. Behm, J. Catal. 269 (2010) 255–268.
[65] A. Gallo, C. Pirovano, M. Marelli, R. Psaro, V. Dal Santo, Chem. Vap. Deposition 16 (2010) 305–310.
[66] X. Xu, C. Zhang, Y. Liu, Y. Zhai, R. Zhang, X. Tang, Environ. Prog. Sustain. Energy 34 (3) (2015) 915–922.
[67] K.A. Resende, C.N. Avila-Neto, R.C. Rabelo-Neto, F.B. Noronha, C.E. Hori, Catal. Today 242 (Part A) (2015) 71–79.
[68] F.G.E. Nogueira, P.G.M. Assaf, H.W.P. Carvalho, E.M. Assaf, Appl. Catal. B: Environ. 160–161 (2014) 188–199.
[69] X. Zhu, P. Huo, Y.-P. Zhang, D.-G. Cheng, C.-J. Liu, Appl. Catal. B: Environ. 81 (2008) 132–140.
[70] W.-Z. Li, L. Kovarik, D. Mei, M.H. Engelhard, F. Gao, J. Liu, Y. Wang, C.H.F. Peden, Chem. Mater. 26 (2014) 5475–5481.
[71] C.T. Campbell, J.R.V. Sellers, Faraday Dis. 162 (2013) 9–30.
[72] N. Scotti, M. Dangate, A. Gervasini, C. Evangelisti, N. Ravasio, F. Zaccheria, ACS Catal. 4 (2014) 2818–2826.
[73] A. Beretta, T. Bruno, G. Groppi, I. Tavazzi, P. Forzatti, Appl. Catal. B: Environ. 70 (2007) 515–524.
[74] A. Beretta, A. Donazzi, G. Groppi, P. Forzatti, V. Dal Santo, L. Sordelli, V. De Grandi, R. Psaro, Appl. Catal. B: Environ. 83 (2008) 96–109.
[75] Y. Xu, C. Fan, Y.A. Zhu, P. Li, Ping, X.-G. Zhou, D. Chen, W.-K. Yuan, Catal. Today 186 (2012) 54–62.
[76] V. Dal Santo, C. Mondelli, V. De Grandi, A. Gallo, S. Recchia, L. Sordelli, R. Psaro, Appl. Catal. A: Gen. 346 (2008) 126–133.